# Numerical Simulation and Industrial Application of High Speed Tandem TIG Welding

**Dongsheng Wu**
Shanghai Jiao Tong University
**Jiuling Huang**
Shanghai Jiao Tong University
**Kong Liang** ( ingerkongliang@sjtu.edu.cn )
Shanghai Jiao Tong University
**Xueming Hua**
Shanghai Jiao Tong University
**Min Wang**
Shanghai Jiao Tong University
**Hua Li**
Zhangjiagang Huayu Nonferrous Metal Material Co.,Ltd, Shanghai
**Shoutian Liu**
Zhangjiagang Huayu Nonferrous Metal Material Co.,Ltd, Shanghai

**Research Article**

**Keywords:** tandem TIG welding, titanium tube, backward flow, arc efficiency

**Posted Date:** July 21st, 2021

**DOI:** https://doi.org/10.21203/rs.3.rs-724082/v1

# Numerical simulation and industrial application of high speed tandem TIG welding

Dongsheng Wu[1], Jiuling Huang[1], Liang Kong[1,*], Xueming Hua[1], Min Wang[1], Hua Li[2] ,Shoutian Liu[2]

1. Shanghai Key Laboratory of Material Laser Processing and Modification (Shanghai Jiao Tong University), Shanghai 200240, PR China

2. Zhangjiagang Huayu Nonferrous Metal Material Co.,Ltd, Shanghai 215627, PR China

* Corresponding author: Liang Kong

Email: ingerkongliang@sjtu.edu.cn

**Abstract**

Self-developed high speed tandem TIG welding equipment were adopted to manufacture titanium welded tubes with high efficiency and high quality. The joint made by this high efficient welding process met Chinese standard requirements. A coupled electrode, arc and weld pool numerical model was also developed to investigate temperature and velocity distributions, and energy propagation of this welding process. The numerical results showed that the Marangoni stress was much higher than the arc shear stress, and was mainly positive after leading and trailing arcs in the x and y directions, so the molten metal flowed backward on the top weld pool surface. Previous studies proposed that a "pull-push" flow pattern defined as a backward molten metal flow after the leading arc and a forward molten metal flow before the trailing arc existed on the top weld pool surface in tandem arc welding processes, while it was not observed in this case. The calculated arc efficiency of the high speed tandem TIG welding was about 79.8%.

**Keywords:** tandem TIG welding, titanium tube, backward flow, arc efficiency

## 1 Introduction

Pure titanium and titanium alloy tubes possess advantages of high strength-to-weight ratios at room temperature and high temperature, high corrosion resistance and high temperature creep resistance [1,2], thus are widely utilized in electric power, marine engineering and petrochemical industries [3,4]. Compared with titanium seamless tubes, titanium welded tubes have similar or same chemical compositions, mechanical properties and process performances, while the production cost is much lower. Usually, tungsten inert gas (TIG) welding is adopted to manufacture titanium welded tubes, while the welding efficiency can't be further improved owing to the formation of weld defects, such as humping and burn through, in high current and high speed cases [5,6].

In order to improve the welding efficiency and quality, a high speed tandem TIG welding process was developed to successfully weld titanium plates in our previous study [7], and is adopted to manufacture titanium welded tubes in this study. In this high efficient welding process, a higher current leading arc aimed to obtain deep penetration, and a lower current trailing arc heated the trailing part of the weld pool, and

suppressed the strong backward molten metal flow [8].

Energy propagation during a non-consumable gas shielded arc welding process plays an important role on the lifetime of a tungsten electrode [9] and final weld bead formation [10]. The main energy propagation mechanisms at the cathode surface are thermionic cooling, thermally conducted energy from the arc column, ion heating and radiation cooling. The main energy propagation mechanisms at the anode surface are electron condensation heating, thermally conducted energy from the arc column, and radiation cooling [11]. Previous studies showed that the maximum arc temperature [12,13] and arc pressure [14,15] in a twin TIG arc were lower in comparison with a single TIG arc with a same total current; therefore, the thermally conducted energy from a twin TIG arc to the cathodes and anode also decreased. As the size of a twin/tandem TIG arc increases, the radiation cooling of the arc column also becomes stronger. Qin et.al [8] and Jiang et.al [16] proposed that an obvious "pull-push" flow pattern defined as backward and forward molten metal flows on the top weld pool surface between two arcs existed in a high speed tandem TIG welding process. This "pull-push" flow pattern might cause more sufficient energy convection, such that the weld cooling rate in a high speed tandem TIG welding process was much higher than that in a TIG welding process. In summary, owing to the coupling effects of leading and trailing arcs, the energy propagation behaviors in a high speed tandem TIG welding process may be significantly different from these in a TIG welding process.

During an arc welding process, the shape of workpiece also affects the arc behaviors as well as energy propagation. Ogino et.al [17,18] investigated the arc behavior and heat input distribution of a TIG arc with a groove surface based on a 3D numerical model, and found that the maximum heat input was located at side surfaces of the groove, and energy efficiency was increased. Dong et.al [19] proposed that in a narrow gap TIG welding process, as the shape of the workpiece surface changed from concave to convex, the arc root shrank, and the energy efficiency was decreased. During the high speed tandem TIG welding of titanium tubes, the anode surface is convex upward, which may also has a great influence on the energy propagation.

In this study, high speed tandem TIG welding equipment were developed to manufacture titanium welded tubes. A coupled electrode, arc and weld pool numerical model was built to investigate temperature and velocity distributions, and energy propagation. Energy balance of the whole welding system was analyzed. Weld microstructures and mechanical properties of the joint were also studied, showing that the high speed tandem TIG welding can improve the manufacturing efficiency and quality of titanium welded tubes.

## 2 Numerical model and numerical simulation

### 2.1 Computational domain and mesh

**Fig.1** shows a three dimensional symmetrical computational domain for a tandem TIG welding process, which includes tungsten electrode regions, nozzle regions, Ar region and titanium tube region. The leading and trailing electrode diameters, electrode spacing, and distance between electrodes and base metal are 3.2

mm, 2.4 mm, 10 mm and 3 mm, respectively. During the welding experiments, the electrodes and nozzles ae stationary, while the titanium tube moves. The maximum top surface deformation under the leading arc is measured by experiment, and the value is 0.55 mm. The bottom reinforcement is about 0.16 mm. A simplified weld pool is predefined in the domain. The titanium tube motion is also considered in our numerical model. A non-uniform mesh system containing a fine mesh region and a coarse mesh region is used: 0.15 mm in electrode tips and the titanium tube, 0.2 mm in the electrode cylinders, 0.25 mm in the Ar region and 0.3 mm in the nozzles in the fine mesh region; 0.3 mm in the titanium tube in the coarse region.

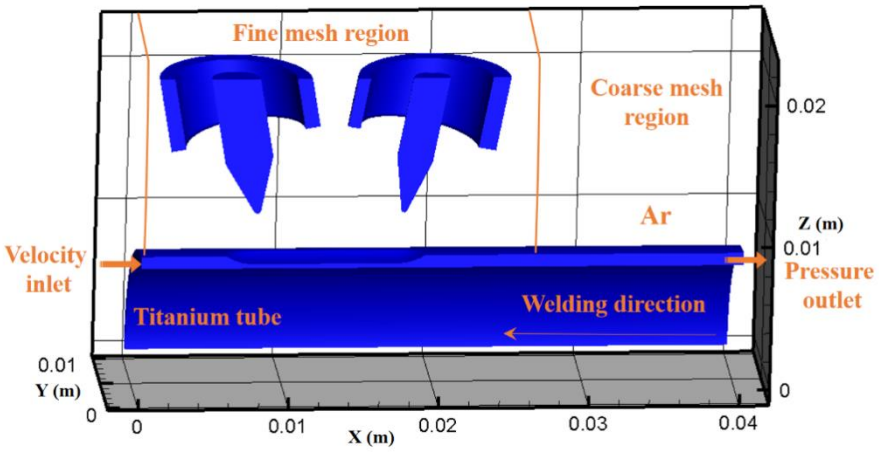


Fig. 1 Computational domain in the numerical model

**2.2 Assumptions, governing equations and boundary conditions**

Many general assumptions are employed to simplify the numerical model for the high speed tandem TIG welding process, such as local thermodynamic equilibrium (LTE) arc plasma [20], Newtonian fluids, turbulent flow of arc and molten metal. The buoyancy force in the molten pool is calculated by Boussinesq approximation and metal vapour effects are neglected [21]. Governing equations for arc and molten pool modeling include the mass, momentum, energy, current and turbulence kinetic energy conservation equations. The assumptions and governing equations as well as some Maxwell's equations were discussed in our previous study of plasma arc welding [22], thus they are not presented here. Some special boundary conditions for the high speed tandem TIG welding of the titanium tube are shown.

The thermionic cooling, thermally conducted energy from the arc column, ion heating and radiation cooling at the cathode surfaces (leading and trailing electrode surfaces) are considered in the energy boundary condition [23].

$$H_c = -|j_e|\varphi_c + |j_i|V_i + k_{eff}\frac{T_g - T_m}{\delta} - \varepsilon_r \alpha {T_m}^4 \quad (1)$$

$$j_e \le j_R = AT_m^2 exp\left(\frac{-e\varphi_{Keff}}{k_B T_m}\right) \quad (2)$$

$$j_e = \begin{cases} j_R & j_R \le |j| \\ |j| & j_R > |j| \end{cases} \quad (3)$$

$$j_i = |j| - j_e \tag{4}$$

where $j_e$ is the electron current density, $j_i$ is the ion current density, $j_R$ is the Richardson current density, $j$ is the total current density, $\psi_c$ is the work function of the cathode, $V_i$ is the ionization potential of argon, $k_{eff}$ is the effective thermal conductivity, $\delta$ is the length of the sheath region, $T_g$ and $T_m$ are the arc temperature and metal temperature at the interface. $\varepsilon_r$ is the surface radiation emissivity, $\alpha$ is the Stefan-Boltzmann constant, A is the Richardson constant, e is the elementary charge, $\psi_{Keff}$ is the effective work function of the electrode, $k_B$ is the Boltzmann's constant.

The electron condensation heating, thermally conducted energy from the arc column, radiation cooling at the anode surface (top titanium tube surface) are considered in the energy boundary condition [24].

$$H_a = |j|\varphi_a + k_{eff}\frac{T_g - T_m}{\delta} - \varepsilon_r \alpha {T_m}^4 \tag{5}$$

where $\psi_a$ is the work function of the anode.

The bottom titanium tube surface can't get any energy from the arc column, so only convective energy transfer and radiation cooling are considered in the energy boundary condition.

$$H_b = -h_{con}(T_m - T_0) \ - \varepsilon_r \alpha {T_m}^4 \tag{6}$$

where $h_{con}$ is the convective heat transfer coefficient, $T_0$ is the ambient temperature.

The Marangoni stress and arc shear stress are considered at the momentum boundary condition of the top weld pool surface in the tangential direction :

$$-\mu\frac{\partial \boldsymbol{v_t}}{\partial \boldsymbol{n}} = \frac{\partial \boldsymbol{\gamma}}{\partial T}\frac{\partial T}{\partial S} - \mu_p\frac{\partial \boldsymbol{v_p}}{\partial \boldsymbol{n}} \tag{7}$$

Only Marangoni stress is considered at the momentum boundary condition of the bottom weld pool surface in the tangential direction:

$$-\mu\frac{\partial \boldsymbol{v_t}}{\partial \boldsymbol{n}} = \frac{\partial \boldsymbol{\gamma}}{\partial T}\frac{\partial T}{\partial S} \tag{8}$$

where $\mu$ is the fluid viscosity, $\boldsymbol{v_t}$ is the tangential fluid velocity, $\boldsymbol{n}$ is the normal vector, $\boldsymbol{S}$ is the tangential vector, $\mu_p$ is the arc plasma viscosity, $\boldsymbol{v_p}$ is the arc plasma velocity.

Table 1. External boundary conditions in the numerical simulation

| Boundary | $\boldsymbol{V}$ | $\boldsymbol{T}$ (K) | $\boldsymbol{\psi}$ (V) | $\boldsymbol{A}$ (T. m) |
|---|---|---|---|---|
| Top leading electrode surface (Wall) | - | 300 | $-\sigma\frac{\partial \varphi}{\partial \boldsymbol{n}} = j_1 = \frac{I_1}{\pi r_1^2}$ | $\frac{\partial \boldsymbol{A}}{\partial \boldsymbol{n}} = 0$ |
| Top trailing electrode surface (Wall) | - | 300 | $-\sigma\frac{\partial \varphi}{\partial \boldsymbol{n}} = j_2 = \frac{I_2}{\pi r_2^2}$ | $\frac{\partial \boldsymbol{A}}{\partial \boldsymbol{n}} = 0$ |
| Top nozzles surfaces (Wall) | - | 300 | $\frac{\partial \varphi}{\partial \boldsymbol{n}} = 0$ | $\frac{\partial \boldsymbol{A}}{\partial \boldsymbol{n}} = 0$ |

| | | | | |
|---|---|---|---|---|
| Shielding gas inlets (Mass flow inlet) | 10 L/min | 300 | $\frac{\partial \varphi}{\partial \boldsymbol{n}} = 0$ | $\frac{\partial \boldsymbol{A}}{\partial \boldsymbol{n}} = 0$ |
| Left titanium tube surface (Velocity inlet) | 5.0 m/min | 300 | $\frac{\partial \varphi}{\partial \boldsymbol{n}} = 0$ | $\frac{\partial \boldsymbol{A}}{\partial \boldsymbol{n}} = 0$ |
| Right titanium tube surface (Pressure outlet) | - | - | $\frac{\partial \varphi}{\partial \boldsymbol{n}} = 0$ | $\frac{\partial \boldsymbol{A}}{\partial \boldsymbol{n}} = 0$ |
| Bottom titanium tube surface (Wall) | - | $-h_{con}\nabla T$ $-\varepsilon_r \alpha T_m^4$ | 0 | 0 |
| Arc out surfaces (Pressure outlet) | - | 300 | $\frac{\partial \varphi}{\partial \boldsymbol{n}} = 0$ | $\frac{\partial \boldsymbol{A}}{\partial \boldsymbol{n}} = 0$ |

where $I_1$ and $I_2$ are leading and trailing electrode currents, $r_1$ and $r_2$ are leading and trailing electrode radii, $j_1$ and $j_2$ are current densities at top leading and trailing electrode surfaces, $\psi$ is the electric potential, $\boldsymbol{A}$ is the vector potential.

## 3 Equipment development and welding procedures

The titanium welded tube manufacturing equipment including a titanium strip feeding equipment, a titanium tube forming equipment, a titanium tube welding equipment, two titanium welded tube calibration equipment, a titanium welded tube annealing equipment and a titanium welded tube cutting equipment were developed by our team, as shown in **Fig. 2**. The titanium strips were exported through a skewed roller in the titanium strip feeding equipment, and were processed into tubes through various types of roll molds in the titanium tube forming equipment. These tubes were welded by the high speed tandem TIG welding, and the sizes were calibrated by a titanium welded tube calibration equipment. In order to eliminate the residual stress after the welding and calibration, the tubes were annealed in the titanium welded tube annealing equipment with annealing temperature of about 580℃; this equipment was filled with pure Ar to protect the tubes from being oxidized. The tubes were calibrated again by another titanium welded tube calibration equipment. The tubes were cut according to buyer's requirements. To ensure the quality of titanium welded tubes, microstructure analysis and mechanical tests were carried out following the GB/T3625-2007 standard.

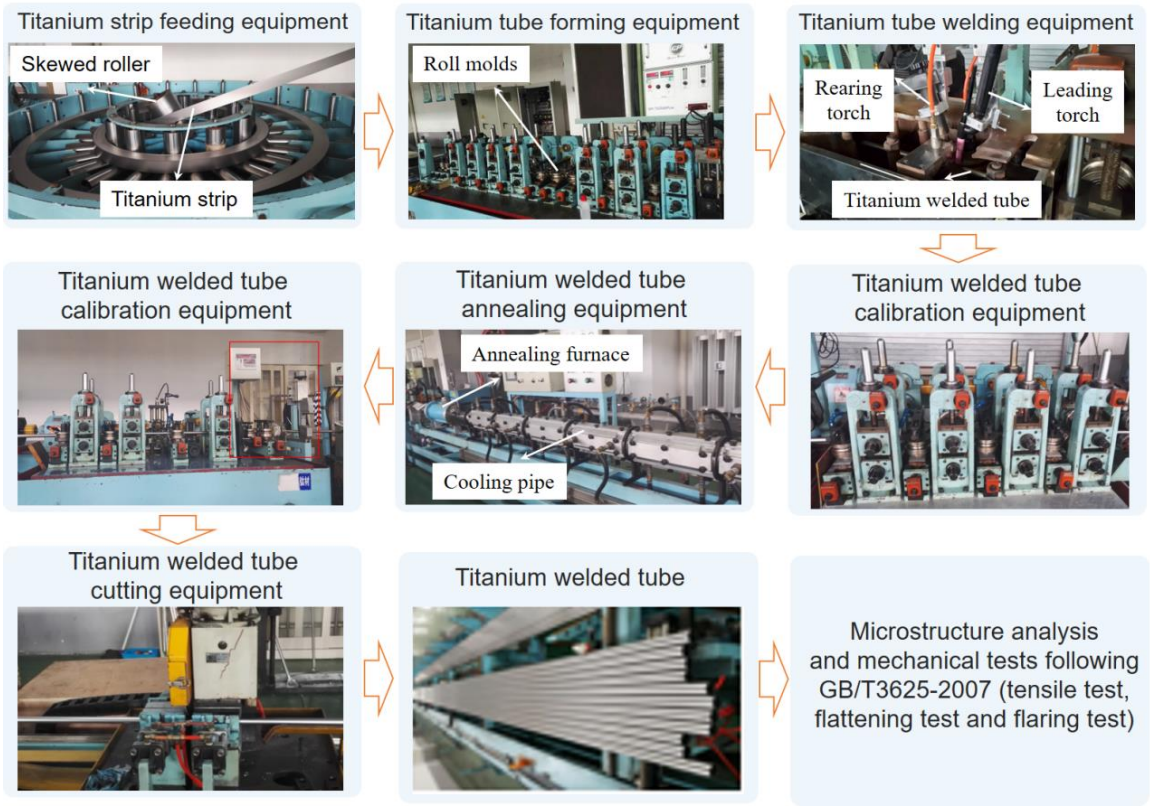


Fig. 2 Manufacturing flowchart of titanium welded tubes

During the welding, a tandem TIG welding power source (MPT-500D) was used. W-$ThO_2$ electrodes was adopted. Pure titanium (TA2) strips with thickness of 0.7 mm were used. The density, thermal conductivity, electrical conductivity, specific heat and viscosity of TA2 were calculated by the JMatpro software, as shown in **Fig. 3**. Other thermo-physical material properties of TA2 can be seen in Table 2. After forming, the tube radius was about 9.55 mm. The leading and trailing TIG torches were fixed, while the titanium tube moved.

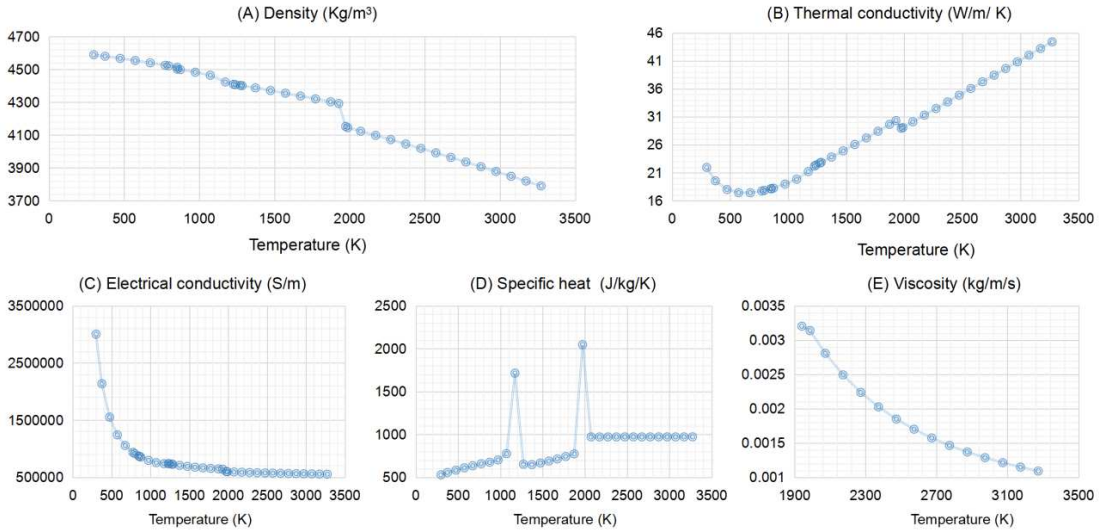


Fig. 3 Thermo-physical material properties of TA2: (A) Density; (B) Thermal conductivity; (C) Electrical conductivity; (D) Specific heat; (E) Viscosity

Table. 2 Thermo-physical material properties of pure titanium (TA2)

| Nomenclature | Value | Nomenclature | Value |
|---|---|---|---|
| Liquidus temperature (K) | 1941.2 | Solidus temperature (K) | 1940.8 |
| Boiling temperature (K) | 3562 | Emissivity | 0.63 |
| Coefficient of thermal expansion($K^{-1}$) | $8.9\times10^{-6}$ | Surface tension gradient (N $m^{-1}$ $K^{-1}$) | -0.00015 |

Detailed welding parameters can be seen in **Table. 3**. A sample of the titanium welded tube is shown in **Fig.4**. Silver-white weld without defects was obtained. The bead was cut, mounted, polished and etched using 5 ml HF + 10 ml $HNO_3$ + 85 ml $H_2O$ solution with 30 s; the weld microstructure was observed using an optical microscope. The tensile test, flattening test and flaring test were carried out following the GB/T3625-2007 standard.

Table. 3 Welding parameters

| Leading / trailing electrode diameters | Leading / trailing tip angle | Electrode height | Electrode spacing | Leading / trailing electrodes angles | Leading /trailing welding currents | Welding speed | Shielding gas flow rate (Ar) |
|---|---|---|---|---|---|---|---|
| 3.2/2.4 mm | 45° /30° | 3.0 mm | 10 mm | 100° / 80° | 160 A / 70 A | 5.0 m/min | 10 l/min |

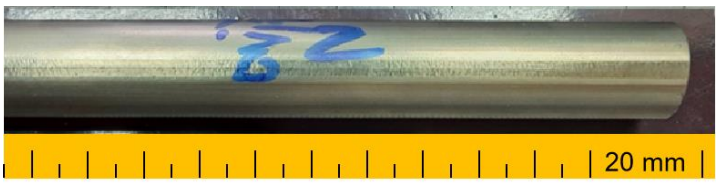


Fig. 4 Titanium welded tube made by high speed tandem TIG welding

# 4 Result and discussion

## 4.1 Temperature and velocity distributions of electrode, arc and weld pool

The temperature distribution of electrode, arc and weld pool in the symmetry plane is shown in **Fig. 5**. In high speed tandem TIG welding, the polarities of leading and trailing electrodes are same, so arcs attract each other under the influence of the electromagnetic force [25]. The maximum arc temperature (17535 K) locates at the region below the leading electrode. The maximum leading electrode temperature and maximum weld pool temperature located at the regions near the leading arc are 3743 K and 3149 K, respectively. Two high temperature regions can be seen in the weld pool.

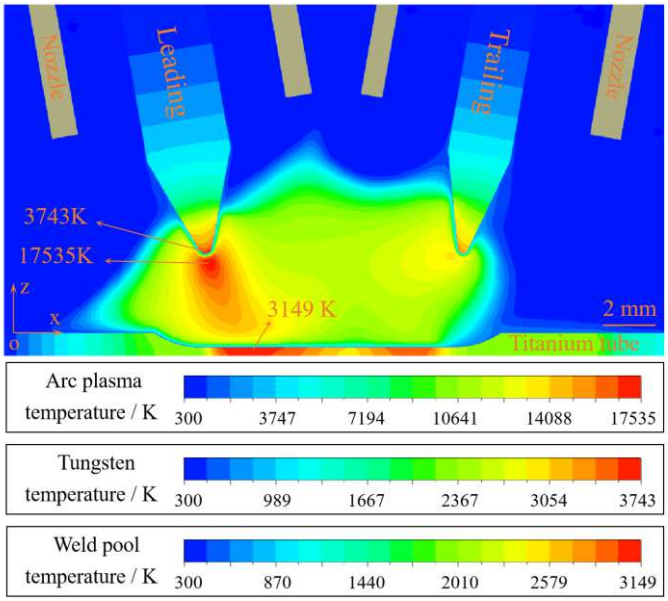


Fig. 5 Temperature distribution of electrode, arc and weld pool in the symmetry plane

As shown in **Fig. 6**, in the symmetry plane, arc plasma under the leading electrode flows downward with a maximum velocity of 226 m/s. After striking the anode surface, arc plasma flows outward parallel to the convex surface, which is similar to the case with a flat surface [26]. As the trailing electrode current is much lower, arc plasma under the trailing electrode firstly flows downward and toward the leading electrode, but then flows upward.

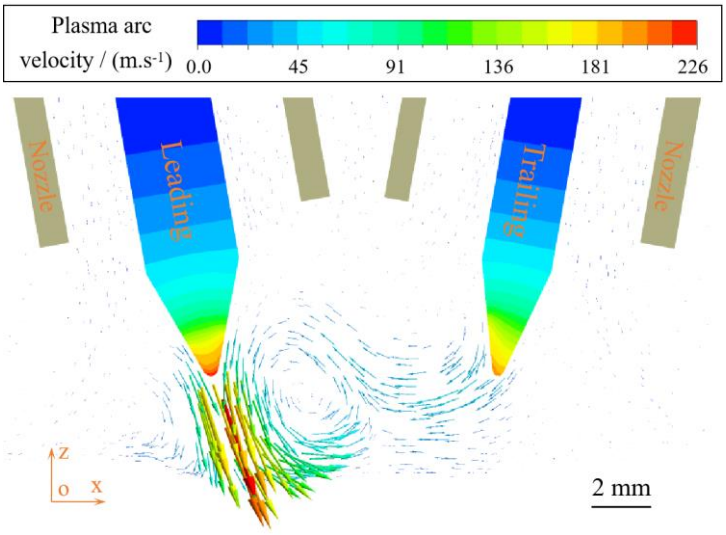


Fig.6 Arc plasma flow in the symmetry plane

As shown in **Fig. 7**, two high temperature regions form at the top weld pool surface under the leading and trailing arcs. The molten metal flows backward behind both leading and trailing arcs with a maximum velocity of 1.04 m/s. Previous studies proposed that a “pull-push” flow pattern defined as a backward molten metal flow after the leading arc and a forward molten metal flow before the trailing arc existed in a high speed tandem TIG weld pool [8,16]. This flow pattern can also be observed in a tandem/twin MIG weld pool [27,28], a TIG-MIG weld pool [29] and a hybrid plasma-MIG pool [30]. However, in our study, the molten metal

mainly flows backward at the top weld pool surface.

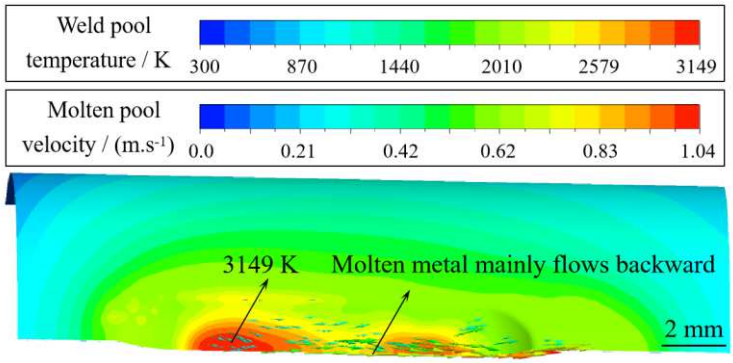


Fig.7 Molten metal temperature and flow on the top weld pool surface

As shown in **Fig. 8**, owing to the outward flow of leading arc plasma, in the x direction, the arc shear stress acting on the top weld pool surface is negative before the leading arc, and positive after the leading arc. Owing to the arc attraction, the trailing arc plasma mainly flows forward, so in the x direction, the arc shear stress acting on the top weld pool surface near the trailing arc is negative. In the y direction, the arc shear stress is mainly positive near both leading and trailing arcs.

In the x direction, the Marangoni stress acting on the top weld pool surface is negative before the leading arc, and mainly positive after leading and trailing arcs. In the y direction, the Marangoni stress acting on the top weld pool surface is mainly positive near both leading and trailing arcs. As the Marangoni stress is much higher than the arc shear stress, it can be concluded that under the influence of the Marangoni stress, the molten metal on the top weld pool surface flows backward.

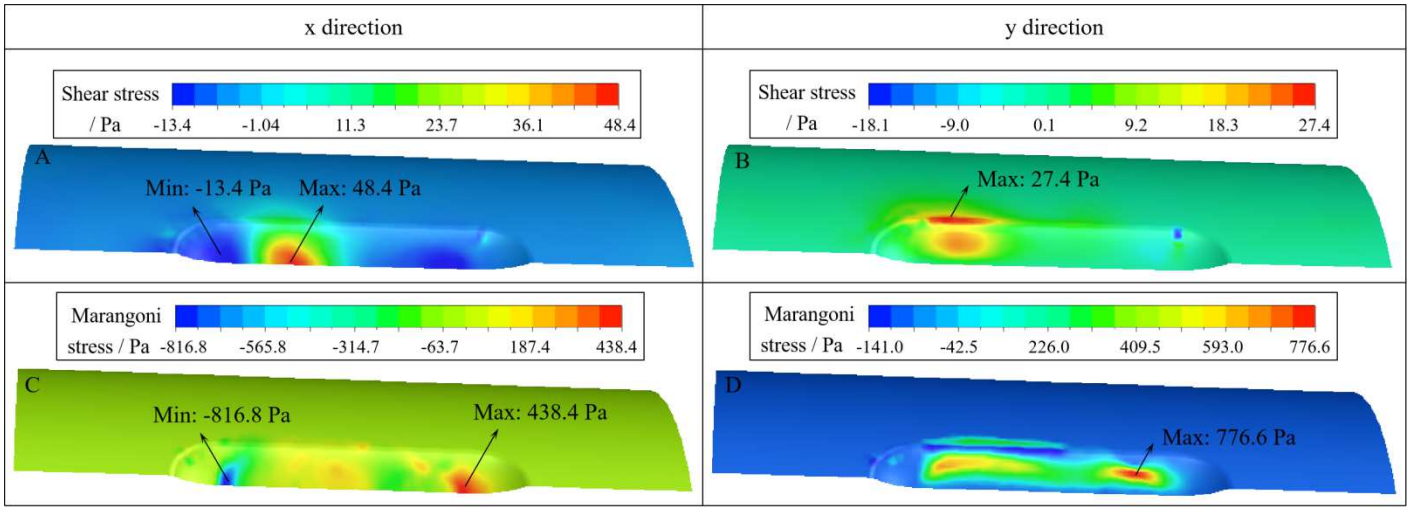


Fig.8 Arc shear stress and Marangoni stress distributions

### 4.2 Arc energy balance and efficiency of the welding system

Energy balance of the whole welding system is shown in **Fig. 9**. For the leading electrode, the joule heat, conduction energy from the arc and ion heating are 13.7 W, 167.5 W and 211.0 W, respectively. The thermionic cooling, conduction energy loss through the electrode top and radiation loss are 238.6 W, 92.4 W and 4.0 W,

respectively. For the trailing electrode, the joule heat, conduction energy from the arc and ion heating are 3.5 W, 59.9 W and 105.7 W, respectively. The thermionic cooling, conduction energy loss through the electrode top and radiation loss are 83.3 W, 55.3 W and 3.0 W, respectively.

For the arc, the joule heat is 1085.5 W. The conduction energy loss to the environment and radiation loss are 195.6 W and 243.8 W, respectively.

For the anode, the joule heat, conduction energy from the arc and thermionic heating are 14.9 W, 411.0 W and 455.4 W, respectively. The radiation loss is 39.4 W.

The calculated arc efficiency of the high speed tandem TIG welding is about 79.8%. Tanaka et.al showed that the calculated TIG arc efficiency was 82% [24]. Stenbacka et.al proposed that the average TIG arc efficiency was about 77% [31]. Based on a calorimetric study of TIG welding of aluminium, Cantin et.al [32] measured the TIG arc efficiency, and found that the arc efficiency in electrode negative polarity (about 80%) is higher than that in electrode positive polarity (about 60%). In summary, the calculated arc efficiency of a tandem TIG arc in this study is reasonable.

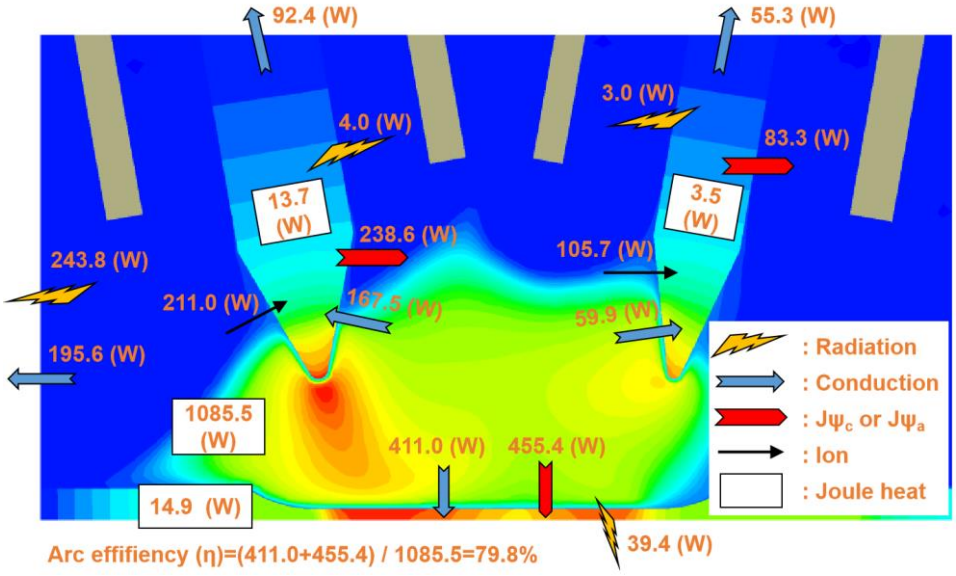


Fig.9 Energy balance and efficiency of the whole welding system

### 4.3 Weld microstructures and mechanical properties

The weld microstructures in the high speed tandem TIG welding are shown in **Fig. 10**. Fine equiaxed α grains exist in the base metal. Jagged grains form in the heat affected zone (HAZ) close to the base metal (region 1 and region2). As shown in region 3, coarser jagged grains form in the HAZ close to the fusion zone (FZ). In the FZ, there are many coarse equiaxed dendrite grains, and a few fine equiaxed dendrite grains.

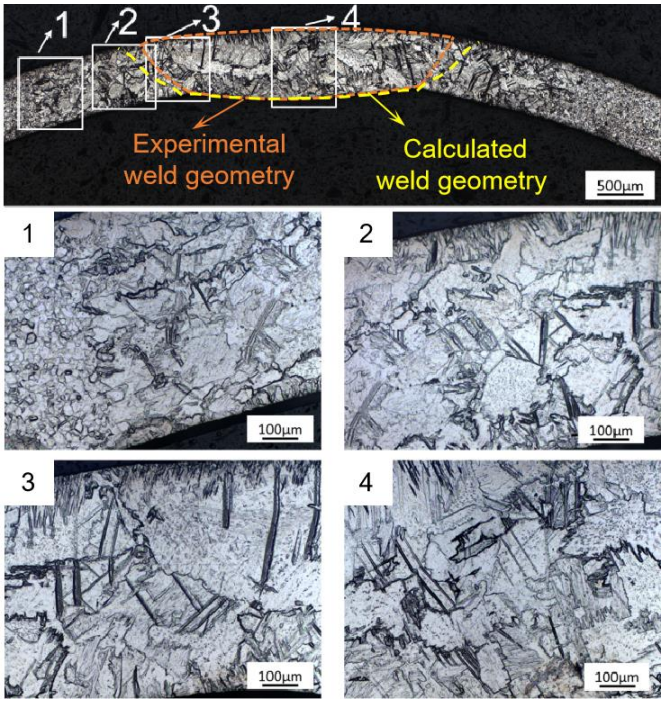


Fig. 10 Weld microstructures in the high speed tandem TIG welding

Both in the numerical simulation and experiment, no weld defect forms in this welding process. As shown in **Fig. 11**, clear necking can be observed in the fracture location. The tensile strength, yield strength and elongation of the bead made by the high speed tandem TIG welding are 458.26Mpa, 357.42 Mpa and 36%, respectively. No crack forms in the weld after flattening test and flaring test. In summary, the joint made by the high speed tandem TIG welding meets the requirements of GB/T3625-2007 standard.

| | Tensile test | Flattening test | Flaring test |
|---|---|---|---|
| High speed tandem TIG welding | 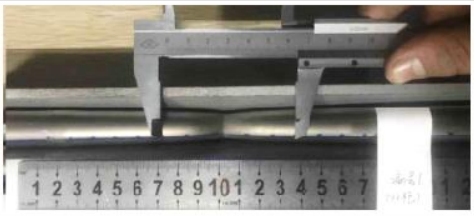 |  |  |

Fig. 11 Mechanical tests of the titanium welded tube

## 5 Numerical simulation validation

Sadek et.al [33] measured the W-$ThO_2$ electrode temperature distribution with a current of 150 A, electrode diameter of 2.4 mm and tip angle of 45 deg, and found the maximum electrode temperature was about 3600 K. Tanaka et.al [11] calculated the temperature and velocity distributions of a TIG arc with a current of 150 A, electrode diameter of 3.2 mm and tip angle of 60 deg, and found the maximum arc temperature was about 17000 K. Haidar et.al [34] found that arc current and cathode tip had great influences on electrode and arc temperature distributions. In this study, with a leading current of 160 A, electrode diameter of 3.2 mm and tip angle of 45 deg, the calculated maximum electrode and arc temperatures are 3743

K and 17535 K, respectively. As shown in **Fig. 10**, the calculated top and bottom weld widths are 3.85 mm and 2.57 mm, respectively. The experimental top and bottom weld widths are 3.39 mm 2.41 mm, respectively. In summary, the calculated arc efficiency, maximum electrode and arc temperatures, and weld geometry are acceptable.

## 6 Conclusions

In this study, titanium tubes were successfully welded by self-developed high speed tandem TIG welding equipment. A coupled electrode, arc and weld pool numerical model was built to investigate temperature and velocity distributions, and energy propagation of this welding process. The following conclusions can be drawn:

(1) The trailing arc current is much lower, under the influence of the electromagnetic force, arc plasma under the trailing electrode firstly flows downward and toward the leading electrode, but then flows upward.

(2) Two high temperature regions locate at the top weld surface, and the "pull-push" flow pattern proposed in previous studies is not formed in this case. The Marangoni stress on the top weld pool surface is mainly positive after leading and trailing arcs in the x and y directions, so the molten metal on the top weld pool surface flows backward.

(3) The calculated arc efficiency of the high speed tandem TIG welding is about 79.8%.

(4) The joint made by the high speed tandem TIG welding meets the requirements of GB/T3625-2007 standard.

## Funding

This research was supported by National Key R&D Program of China (No.2016YFB0301205).

## Conflicts of interest

The authors have no financial or proprietary interests in any material discussed in this article.

## Availability of data and material

All data supporting the findings of this study are available within the article.

## Code availability

Not applicable.

## Ethics approval

The work contains no libelous or unlawful statements, and does not infringe on the rights of others, and does not contain any materials or instructions that might cause harm or injury.

## Consent to participate

All authors consent to participate.

## Consent for publication

All authors agree to publish.

## Authors' contributions

All authors have participated in the conception, design, analysis, and interpretation of the data as well as the writing, drafting, and revising of the article.

## Reference

[1] Shokrani, A., Dhokia, V., & Newman, S. T. (2016). Investigation of the effects of cryogenic machining on surface integrity in CNC end milling of Ti–6Al–4V titanium alloy. Journal of Manufacturing Processes, 21, 172-179.

[2] De Oliveira, J. A., Ribeiro Filho, S. L. M., Lauro, C. H., & Brandão, L. C. (2017). Analysis of the micro turning process in the Ti-6Al-4V titanium alloy. The International Journal of Advanced Manufacturing Technology, 92(9), 4009-4016.

[3] Veiga, C., Davim, J. P., & Loureiro, A. J. R. (2012). Properties and applications of titanium alloys: a brief review. Reviews on Advanced Materials Science, 32(2), 133-148.

[4] Mahamood, R. M., & Akinlabi, E. T. (2018). Corrosion behavior of laser additive manufactured titanium alloy. The International Journal of Advanced Manufacturing Technology, 99(5), 1545-1552.

[5] Meng, X., Qin, G., & Zou, Z. (2016). Investigation of humping defect in high speed gas tungsten arc welding by numerical modelling. Materials & Design, 94, 69-78.

[6] Abbasi, Z., Yuhas, D., Zhang, L., Basantes, A. D. C., Tehrani, N., Ozevin, D., & Indacochea, E. (2018). The detection of burn-through weld defects using noncontact ultrasonics. Materials, 11(1), 128.

[7] Huang, J., Kong, L., Wang, M., Wu, D., & Li, F. (2019). Pure titanium TA2 thin plate double tungsten electrode argon arc welding process [J]. Transactions of the China Welding Institution, 40(9),14-18.

[8] Qin, G., Meng, X., & Fu, B. (2015). High speed tandem gas tungsten arc welding process of thin stainless steel plate. Journal of Materials Processing Technology, 220, 58-64.

[9] Liu, Z., Fang, Y., Chen, S., Zhang, T., Lv, Z., & Luo, Z. (2019). Focusing cathode tip characteristics in cooling tungsten. Energy, 167, 982-993.

[10] Van Anh, N., Wu, D. S., Tashiro, S., Hua, X. M., & Tanaka, M. (2019). Undercut formation mechanism in the keyhole plasma arc welding. Welding Journal, 98, 204s-212s.

[11] Tanaka, M., Yamamoto, K., Tashiro, S., Nakata, K., Yamamoto, E., Yamazaki, K., Lowke, J. J. (2010). Time-dependent calculations of molten pool formation and thermal plasma with metal vapour in gas tungsten arc welding. Journal of Physics D: Applied Physics, 43(43), 434009.

[12] Wang, X., Fan, D., Huang, J., & Huang, Y. (2015). Numerical simulation of heat transfer and fluid flow in double electrodes TIG arc-weld pool. Acta Metallurgica Sinca, 51(2), 178-190.

[13] Nomura, K., Shirai, K., Kishi, T., & Hirata, Y. (2015). Study on temperature measurement of two-electrode TIG arc plasma. Welding International, 29(7), 493-501.

[14] Leng, X., Zhang, G., & Wu, L. (2006). The characteristic of twin-electrode TIG coupling arc

pressure. Journal of Physics D: Applied Physics, 39(6), 1120.
[15] Schwedersky, M. B., Gonçalves e Silva, R. H., Dutra, J. C., Reisgen, U., & Willms, K. (2016). Two-dimensional arc stagnation pressure measurements for the double-electrode GTAW process. Science and Technology of Welding and Joining, 21(4), 275-280.
[16] Jiang, H., Qin, G., Feng, C., & Meng, X. (2019). High-speed tandem pulsed GTAW of thin stainless steel plate. Welding Journal, 98(8), 215s-226s.
[17] Ogino, Y., Hirata, Y., & Nomura, K. (2011). Heat input and pressure distribution of TIG arc on groove surface. Welding in the World, 55(11), 107-113.
[18] Ogino, Y., Nomura, K., & Hirata, Y. (2013). Numerical analysis of arc plasma behaviour in groove welding with 3D TIG arc model. Welding International, 27(11), 867-873.
[19] Dong, B., Cai, X., Ni, Z., Lin, S., Fan, C., & Yang, C. (2019). Numerical simulation of arc characteristics in narrow gap TIG welding. International Journal of Mechanical Sciences, 161, 105031.
[20] Tanaka, M., Ushio, M., & Lowke, J. J. (2004). Numerical study of gas tungsten arc plasma with anode melting. Vacuum, 73(3), 381-389.
[21] Ogino, Y., Hirata, Y., Kawata, J., & Nomura, K. (2013). Numerical analysis of arc plasma and weld pool formation by a tandem TIG arc. Welding in the World, 57(3), 411-423.
[22] Wu, D., Tashiro, S., Hua, X., & Tanaka, M. (2021). Coupled mechanisms of the keyhole, energy transfer and compositional change associated with the variable polarity plasma arc process. Journal of Physics D: Applied Physics, 54(11), 115204.
[23] Liu, Z., Li, Y., & Su, Y. (2018). Simulation and analysis of heat transfer and fluid flow characteristics of arc plasma in longitudinal magnetic field-tungsten inert gas hybrid welding. The International Journal of Advanced Manufacturing Technology, 98(5), 2015-2030.
[24] Dong, B., Cai, X., Lin, S., Ni, Z., & Fan, C. (2021). Numerical simulation on the nonaxisymmetry arc characteristics in narrow gap TIG welding: responses to welding parameters. The International Journal of Advanced Manufacturing Technology, 114(7), 2229-2242.
[25] Wang, X., Fan, D., Huang, J., & Huang, Y. (2015). Numerical simulation of arc plasma and weld pool in double electrodes tungsten inert gas welding. International Journal of Heat and Mass Transfer, 85, 924-934.
[26] Lago, F., Gonzalez, J. J., Freton, P., & Gleizes, A. (2004). A numerical modelling of an electric arc and its interaction with the anode: Part I. The two-dimensional model. Journal of Physics D: Applied Physics, 37(6), 883.
[27] Ueyama, T., Ohnawa, T., Tanaka, M., & Nakata, K. (2005). Effects of torch configuration and welding current on weld bead formation in high speed tandem pulsed gas metal arc welding of steel sheets. Science and Technology of Welding and Joining, 10(6), 750-759.
[28] Wu, D., Hua, X., Ye, D., & Li, F. (2017). Understanding of humping formation and suppression mechanisms using the numerical simulation. International Journal of Heat and Mass Transfer, 104, 634-643.

[29] Zong, R., Chen, J., & Wu, C. (2019). A comparison of TIG-MIG hybrid welding with conventional MIG welding in the behaviors of arc, droplet and weld pool. Journal of Materials Processing Technology, 270, 345-355.
[30] Wu, D., Tashiro, S., Wu, Z., Nomura, K., Hua, X., & Tanaka, M. (2020). Analysis of heat transfer and material flow in hybrid KPAW-GMAW process based on the novel three dimensional CFD simulation. International Journal of Heat and Mass Transfer, 147, 118921.
[31] Stenbacka, N. (2013). On arc efficiency in gas tungsten arc welding. Soldagem & Inspeção, 18(4), 380-390.
[32] Cantin, G. M. D., & Francis, J. A. (2005). Arc power and efficiency in gas tungsten arc welding of aluminium. Science and Technology of welding and joining, 10(2), 200-210.
[33] Sadek, A. A., Ushio, M., & Matsuda, F. (1990). Effect of rare earth metal oxide additions to tungsten electrodes. Metallurgical transactions A, 21(12), 3221-3236.
[34] Haidar, J., & Farmer, A. J. D. (1995). Surface temperature measurements for tungsten-based cathodes of high-current free-burning arcs. Journal of Physics D: Applied Physics, 28(10), 2089.